Enhanced in-plane magnetic anisotropy in thermally treated arrays of Co-Pt nanowires

Fernando Meneses[1,2,3], Cristina Bran[3], Manuel Vázquez[3], Paula G. Bercoff[1,2 *]
1 Facultad de Matemática, Astronomía, Física y Computación, Universidad Nacional de Córdoba. Córdoba, Argentina.
2 Instituto de Física Enrique Gaviola, CONICET. Córdoba, Argentina.
3 Instituto de Ciencia de Materiales de Madrid, CSIC.28049 Madrid. Spain.

*Corresponding author: bercoff@famaf.unc.edu.ar

Abstract
Ordered arrays of Co_xPt_{100-x} cylindrical nanowires (NWs) with *x*=90, 80, 70 were synthesized by template-assisted electrodeposition using nanoporous alumina membranes of 55 nm pore diameter. The obtained NWs alloys crystallize in *hcp* and/or *fcc* structures, depending on the composition and thermal treatment, resulting in different magnetic behaviors. The magnetic anisotropy was studied as a function of composition and crystalline structure in as-deposited and annealed samples. An enhanced coercivity was obtained for the $Co_{70}Pt_{30}$ NWs array, in which in-plane anisotropy (e.g., perpendicular to the NWs axis) was found. These characteristics have not been reported for NWs of this kind. A simplified model of effective anisotropy including shape, magnetostatic interaction and magnetocrystalline contributions is presented, which appropriately describes the magnetic behavior of the Co_xPt_{100-x} NWs arrays before and after annealing.

Keywords: Co-Pt alloys; Cylindrical Nanowires Arrays; Magnetic Anisotropy.

1. Introduction

Magnetic anisotropy is a key magnitude of ferromagnetic materials that determines their magnetic response in the presence of a magnetic field. Its origin is connected to the spin-orbit coupling at the atomic scale whose local symmetry is mainly determined by the composition of the material under consideration. Anisotropic magnetic materials are used in high-density magnetic recording applications [1–3], magneto-optic recording [4–6], micro- and nano-electromechanical devices (MEMS/NEMS) [7,8], magnetic actuators [9,10], sensors [11,12], spin valves [13,14], among others. In planar systems, sometimes perpendicular or out-of-plane anisotropy is desired, like in the case of high-density magnetic recording media. However, for a wide variety of applications it is convenient to engineer the magnetization easy direction defined by the magnetic anisotropy.

As a result of the investigation on hard magnetic materials, Co-based systems have improved with the addition of 4d or 5d noble metals, like Pd or Pt, respectively. The attribute of these alloys is the high magnetic moment–provided by Co– combined with the enhancement of the magnetic anisotropy, originated in the coupling of the Co-3d band with the noble metal 4d/5d band, which improves the orbital moments [15–17]. Particularly, when looking for highly anisotropic materials, Co-Pt alloys are better suited than Co-Pd or Co-X alloys, where X represents a 5d noble metal other than Pt [15,17].

Upon technological advances, Co-Pt-based devices have evolved from 3D bulk geometries [18,19] to low-dimensional nanostructures, like 2D thin films [20–22], 1D nanowires [23–25] and 0D nanoparticles [26–28]. The magnetic properties of these structures are strongly affected by the magnetic anisotropy, which can be considered as coming from different contributions. For example, for 0D nanostructures the magnetocrystalline anisotropy and the size of the particles are determinant features to control the magnetic properties [29,30]. In the case of higher dimensionality systems, shape anisotropy is also present, increasing possibility of tuning the magnetic anisotropy.

For 1D-like NWs arrays, the confinement to one dimension promotes the growth of crystalline phases and many synthesis methods are possible. For instance, thermal decomposition [31], solvothermal synthesis [25], and electrochemical routes like direct current (DC) [23,24,32–37] template-assisted electrodeposition. Electrochemistry has the advantage of employing simple and less-expensive equipment, while the suitable modification of its parameters offers a great versatility to control the geometry and composition of the NWs arrays.

Many authors have studied arrays of metallic NWs and obtained different results regarding the magnetization easy axis of the system. When the diameter of the wires is larger than 100 nm it is possible to design the magnetic anisotropy to be in-plane, out of plane or negligible (isotropic) [32,34,38]. The same versatility is possible when working with Co-Pt thin films [20,39,40]. However, in the case of Co-Pt NWs arrays with diameter smaller than 100 nm, only out-of-plane magnetic anisotropy (that is, parallel to the NWs axis) has been reported [23,36,41–43]. This geometrical aspect limits the applicability of nanowires with diameters ≤ 100 nm, which usually display larger coercivities than thicker ones and thin films, because of geometrical confinement [24].

In this work, cylindrical Co_xPt_{100-x} NWs arrays with x=90, 80, 70 and diameter of 55 nm were synthesized by DC electrodeposition using nanoporous alumina membranes as templates. The magnetic anisotropy was studied as a function of composition and crystalline structure in as-deposited samples and after thermal treatments. In-plane anisotropy (e.g., perpendicular to the NWs axis) was found for the $Co_{70}Pt_{30}$ array, in which an enhanced coercivity was obtained, when comparing with Co-Pt arrays of thicker wires (diameter ≥ 100 nm) and thin films of compositions ranging from $Co_{90}Pt_{10}$ to $Co_{40}Pt_{60}$ [22,32,34,38,39,44–46].

2. Samples preparation and processing

The preparation of the Anodic Aluminum Oxide (AAO) templates was carried out by a two-step anodization process, as described previously [47,48]. These structures are characterized by an ordered hexagonal arrangement of cylindrical pores, with diameter d_{pore} = (55±5) nm, interpore distance (between pore centers) dcc_{pore} = (110±10) nm and length L_{pore} = (40±2) µm. A 200 nm thick gold layer is sputtered on one side of the template to make the electrical contact for electrodeposition. Figure 1 (a) (left) shows a top view of an AAO template.

Electrodeposition of Co-Pt NWs was performed with a 0.015 M K_2PtCl_6 + 0.3 M $CoSO_4$ + 0.2 M H_3BO_3 solution, pH = 3.3, in a three-electrode cell. All the reagents were of analytical grade from Sigma-Aldrich. Since Co and Pt have very different reduction potentials (-0.28 V and 1.18 V *vs*. SHE at 25 ºC and 1 atm, respectively [49]), the electrodeposition potential V was used to control the Co/Pt atomic ratio. The dependence of the composition Co_xPt_{100-x} with V is non-linear, and for x = 90, 80, 70 it was necessary to apply V = -0.8, -0.6 and -0.5 V (measured against a Ag/AgCl reference electrode), respectively. The electrodeposition time was fixed to 15 min because longer times led to irregular growing, generating a Pt deposition on the template's surface instead of within the pores.

After structural and magnetic characterization of the as-deposited samples, the NWs arrays were thermally treated looking for the stabilization of metastable phases and/or phase transitions. The annealing processes were carried out in a GSL-1700X furnace under Ar atmosphere with a +10 ºC/min ramp from room temperature to 500 ºC, 3 hours waiting time, and a -10 ºC/min ramp to reach back room temperature.

3. Structural and magnetic characterization

The synthesized NWs arrays were morphologically characterized with a Sigma Zeiss Field Emission Scanning Electron Microscope (FE-SEM).The NWs diameter d and center-to-center distance dcc were pre-determined by the template (as verified from several SEM images), $d = d_{pore}$ = (55±5) nm and $dcc = dcc_{pore}$ = (110±10) nm. Despite having the same electrodeposition time, the NWs length L was different for each array because the electrodeposition potential V strongly affected the growing dynamics. For the lower values V = -0.6 V and -0.5 V, the length was approximately 4 µm, while for V = -0.8 V it was $L\sim$ 16 µm. In all cases, the length-to-diameter ratio or aspect ratio $Ar = L/d$ is large (≥ 70).

The samples were labeled according to the Co content and whether they were annealed or not. For example, Co**90**-AD and Co**90**-TT represent the as-deposited (AD) and thermally treated (TT) $Co_{90}Pt_{10}$ sample, respectively. Table 1 summarizes the morphological parameters of the as-deposited samples.

Table 1. Morphological and compositional parameters of the as-deposited nanowires arrays, with diameter d = (55±5) nm and interpore distance dcc = (110±10) nm.

Sample	Length L [µm]	Aspect Ratio Ar	Co at.%	Pt at.%
Co**90**-AD	16±1	290±30	90±3	10±3
Co**80**-AD	4±1	70±20	80±3	20±3
Co**70**-AD	4±1	70±20	70±3	30±3

Figure 1 (a) (right) is a close-up SEM image of Co**80**-TT NWs within the AAO membrane, representative of all the arrays deposited in the template shown at the left side of this figure. Figure 1 (b) displays a SEM cross-section image of Co**70**-AD (left) and Co**70**-TT (right) NWs arrays. Single Co**80**-AD and Co**80**-TT nanowires on a silicon substrate, released from the template by chemical procedures are shown in Figure 1 (c) (left and right, respectively). Lastly, Figure 1 (d) (left) shows a backscattered electron (BSE) cross-section view of sample Co**90**-AD, in which the NWs, deposited Au layer and alumina template are visible, while a SEM image of the same array after thermal treatment is shown on the right. Comparison of the AD and TT samples indicates that the thermal treatment does not alter the morphology of the wires.

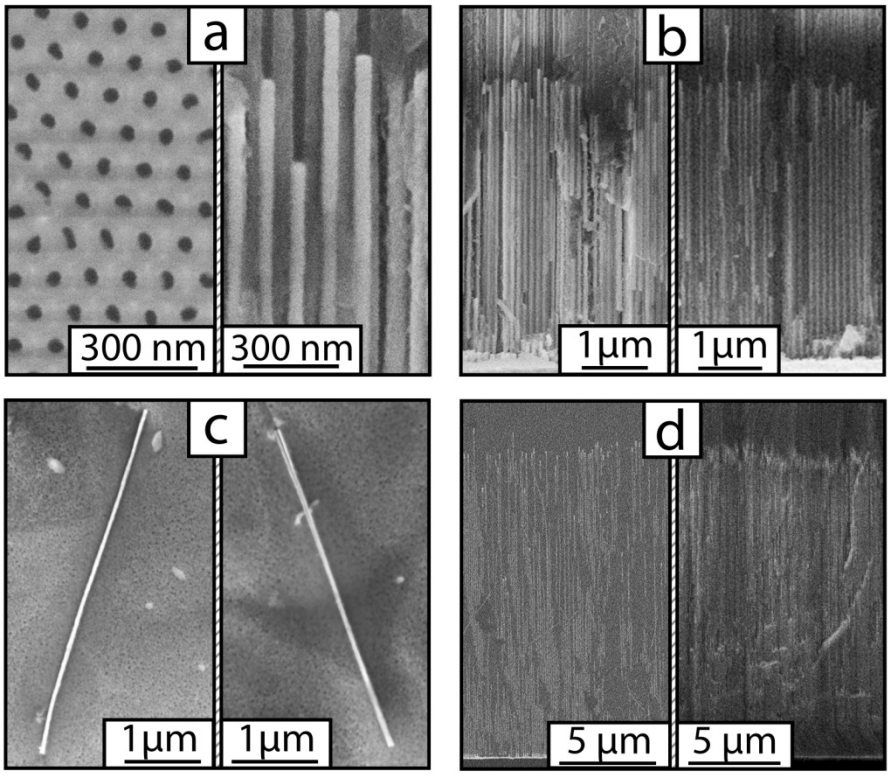

Figure 1. SEM images of: (a) top view of an AAO template (left) and Co**80**-AD NWs. (b) Cross-section view of sample Co**70**-AD (left) and Co**70**-TT (right). (c) Single Co**80**-AD (left) and Co**80**-TT (right) nanowire released from the template. (d) BSE cross-section view of sample Co**90**-AD (left) and SEM image of Co**90**-TT (right).

The elemental compositions Co_xPt_{100-x} were measured for each sample with an Energy Dispersive Spectrometer (EDS) model APOLLO 10 SSD. Cobalt atomic contents x = 90, 80, 70 were found for the voltages -0.8 V, -0.6 V and -0.5 V, respectively (see Table 1). Figure 2 shows an elemental map from a section of the template corresponding to sample Co**90**-AD. The compositional distribution is clearly distinguished, and the alumina template is visible all across the length. In all investigated samples, Co and Pt are homogeneously distributed along the NWs length. The last few nanometers of the topmost segments present almost pure Pt tips, which may be a consequence of the potential cut off during the last stage of the electrodeposition. The tips protect the wires against oxidation while do not contribute to the magnetic behavior.

After annealing, not only the morphology remained unchanged (as seen in Figure 1) but also the composition, as determined by EDS studies.

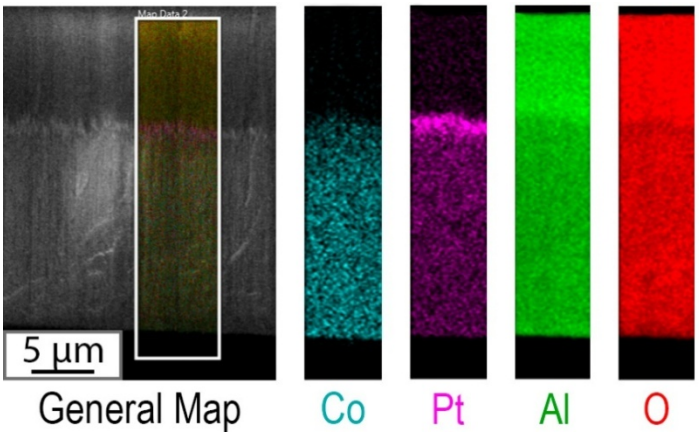

Figure 2. Elemental EDS map of a section of a NWs array, corresponding to sample Co**90**-AD, where the nanowires and the alumina template are clearly distinguished.

3.1 Crystalline Structure

The phase diagram for Co-Pt bimetallic alloy is well known for the bulk materials [50]. In the present study, the composition of the samples ($Co_{90}Pt_{10}$, $Co_{80}Pt_{20}$ and $Co_{70}Pt_{30}$) and the annealing temperature (500 ºC) limit the working zone to the region shown in Figure 3, where only two crystalline phases are possible: cubic *fcc* (αCo,Pt) or hexagonal *hcp* (εCo). The *hcp* phase is more favorable when the Co content is high, above 90 at.% for temperatures below 600 ºC. At at.% Co ≤ 80 and room temperature, the *hcp* phase becomes metastable whereas the *fcc* phase is energetically convenient [18,19,50]. The thermal evolution for each sample is indicated in the figure.

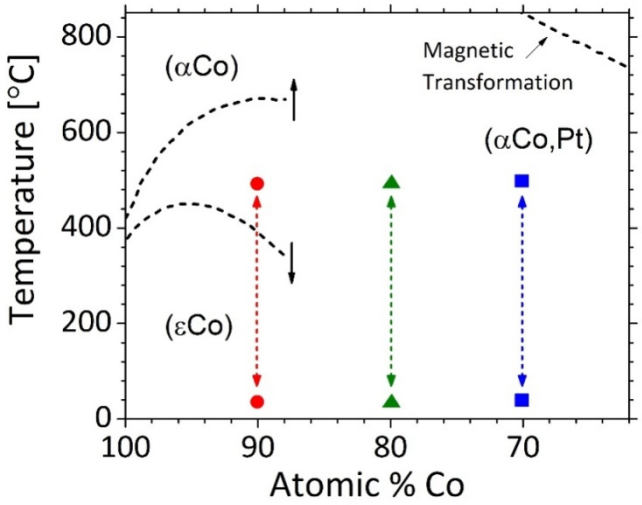

Figure 3. Co-Pt phase diagram in the working zone according to the obtained Co-Pt alloy compositions and annealing temperature (adapted from Reference [50]). The thermal evolution is indicated for each composition (synthesis at room temperature and annealing at 500 ºC).

The crystalline structure of the samples was determined by wide-angle X-Ray Diffraction (XRD), performed with a Panalytical X'Pert Pro device, Cu long-fine focus PIXcel 1D detector, Cu K_α radiation (λ = 1.5419 Å) and instrumental width 0.02º. For these measurements, the NWs arrays embedded in the amorphous AAO templates were placed on a SiO_2 sample holder. The XRD patterns of all samples are shown in Figure 4, where left and right panels correspond to as-deposited and thermally treated samples, respectively.

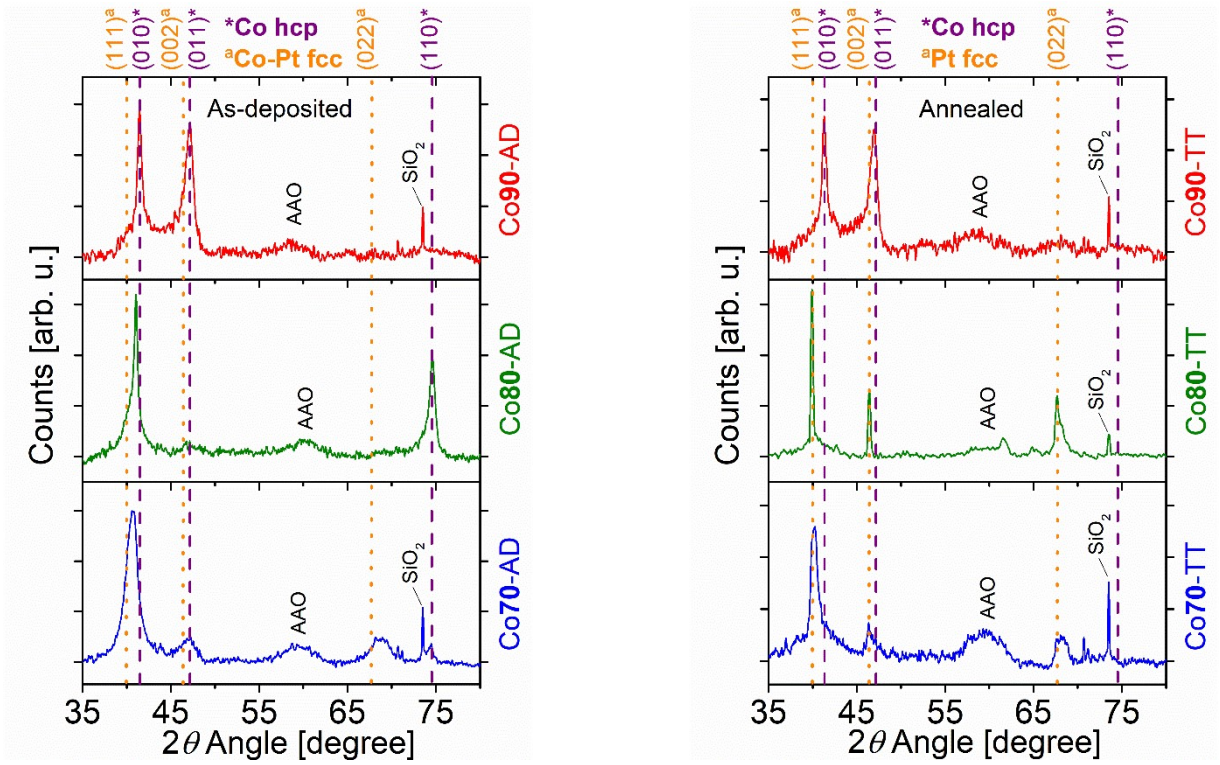

Figure 4. XRD patterns for as-deposited (left) and thermally treated (right) samples, with compositions $Co_{90}Pt_{10}$, $Co_{80}Pt_{20}$ and $Co_{70}Pt_{30}$. The vertical dotted lines (orange) correspond to the Pt *fcc* angular reflections, whereas the dashed lines (violet) belong to the Co *hcp* phase. The alumina and SiO_2 sample holder present a broad peak at 60º and a sharp one at 73º, respectively.

Before and after annealing, all the samples have polycrystalline structures. The Scherrer crystallite size d_S [51] was calculated using the peak with the highest intensity of each pattern, (010) for hcp and (111) for fcc structures. The obtained values are d_S = 10-20 nm in every case, except in sample Co**80**-TT which shows a slight increase (30 nm). The lattice constants were experimentally determined from the Bragg's law and the geometry of each lattice [52], except for samples Co**80**-AD and Co**70**-AD due to the superposition of peaks in the *hcp* and *fcc* phases. The crystallographic texture was calculated from a comparison with powder diffraction patterns [53]. Table 2 presents these crystalline properties.

Table 2. Crystalline properties of all samples. The *hcp* / *fcc* notation indicates that the two crystallographic phases coexist. The associated textures and lattice parameters are also indicated.

Sample	Phase	d_S [nm]	a_{exp} [Å] [±0.01Å]	c_{exp} [Å] [±0.01Å]	Texture
Co**90**-AD	*hcp*	10	2.48	4.13	(010),(011)
Co**90**-TT	*hcp*	10	2.48	4.14	(010),(011)
Co**80**-AD	*hcp* / *fcc*	20	2.50 / -	-	(010) / (111)
Co**80**-TT	*fcc*	30	3.85	*c* =*a*	None
Co**70**-AD	*hcp* / *fcc*	10	2.50 / -	-	-
Co**70**-TT	*fcc*	10	3.84	*c* =*a*	(111)

As expected from the phase diagram, sample Co**90**-AD crystallized in the Co *hcp* phase (PDF 96-901-1616) and remained unaltered after the thermal treatment (Co**90**-TT). It is possible that some Pt *fcc* grains are segregated in both cases, broadening the *hcp* peaks. The experimentally determined lattice constants are a_{exp} = (2.48±0.01) Å and c_{exp} = (4.13±0.01) Å for the basal and longitudinal directions, respectively, in both samples.

These values are close to the pure Co *hcp* lattice $a_{Co\text{-}hcp}$ = 2.507 Å and $c_{Co\text{-}hcp}$ = 4.069 Å [49], and the difference may arise from the bimetallic alloy or the peak broadening. The crystallographic texture is strong in both (010) and (011) *hcp* directions while the diffraction peak corresponding to the (002) *hcp* plane reflection (at 44.486º) is missing. Therefore, there are no crystals oriented with the "*c*" axis of the hexagonal lattice parallel to the NWs axis, being most of the grains oriented along the (010) and (011) directions, as shown schematically in Figure 5.

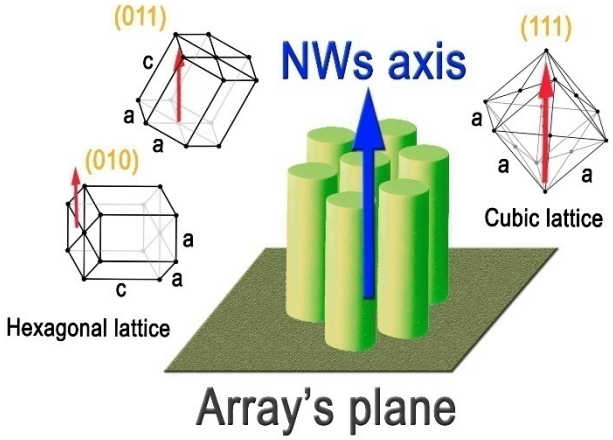

Figure 5. Scheme of the ordered NWs within the template, indicating the direction of the NWs axis and the array's plane. Representative crystallographic images of *hcp* (left) and *fcc* (right) crystals are also displayed, positioned according to the observed textures in the samples. The arrows denote the NWs axis orientation.

In the case of sample Co**80**-AD, the peak at 74.587º corresponds to the (110) *hcp* reflection, and the one at 41.044º is very close to the (010) *hcp* direction, but also has a small contribution from the (111) Pt *fcc* reflection (PDF 96-901-3418). That is consistent with the metastability of the *hcp* phase for this composition at room temperature, and because this sample is not annealed, most of the grains are still in the hexagonal phase. Only the basal lattice constant a_{exp} = (2.50±0.01) Å for the *hcp* structure could be determined from the (110) *hcp* reflection. The crystallographic texture is associated to the (110) and (010) directions of the *hcp* phase, indicating that the "*c*" axis lays in the plane of the array for all grains, that is, perpendicular to the NWs axis.

After annealing, sample Co**80**-TT crystallized in the Pt *fcc* phase, accordingly with the phase diagram, with no crystallographic texture. There are no reflections corresponding to the *hcp* planes from Co, evidencing that Co and Pt are alloyed and the previous Co *hcp* and Pt *fcc* segregation disappeared. The lattice constant a_{exp}= (3.85±0.01) Å is close to the pure Pt value a_{Pt} = 3.912 Å [54].

Similarly to Co**80**-AD, sample Co**70**-AD also displays two contributions to the XRD pattern from the Co *hcp* and Pt *fcc* phases. As a result of the *hcp* and *fcc* peaks superposition, the reflections centered at 40.720º and 47.164º are quite broad. However, it is possible to verify that this sample is at least partially alloyed, because the *fcc* reflections are shifted with respect to the pure Pt lattice, as it can be observed in the (022) *fcc* reflection. The basal *hcp* lattice constant a_{exp} = (2.50±0.01) Å was determined from the small (110) *hcp* reflection. Due to the superposition of crystallographic phases there is no information about the other lattice parameters and an exact description of the crystallographic texture cannot be assessed.

After the thermal treatment, sample Co**70**-TT adopts the Pt *fcc* structure, in agreement with the phase diagram, yet probably some Co *hcp* grains remain, according to the broad peaks at 40.231º and 46.349º. A crystallographic texture in the (111) direction is observed. The lack of intense peaks associated to the Co *hcp* phase confirms that Co and Pt are alloyed. The lattice constant is a_{exp} = (3.84±0.01) Å, similar to sample Co**80**-TT.

3.2 Magnetic Properties

The magnetic properties of the NWs arrays were determined in a Vibrating Sample Magnetometer (VSM, model ADE system EV7 KLATencor) with $\mu_0 H^{MAX}$ = ±1.8 T (being H^{MAX} the maximum applied field). The coercivity H_C and relative remanence m_R=M_R/M_S, (M_R=remanent magnetization; M_S=saturation magnetization) were obtained by analyzing the hysteresis loops before and after annealing. These measurements were carried out in a complete range of angles between the applied field ***H*** and the NWs axis, from 0º to 180º, being θ=0º the

configuration of ***H*** parallel to the NWs axis (i.e., out of plane) and θ=90º the perpendicular orientation (in the plane of the membrane).

Figure 6 shows θ=0º and θ=90º hysteresis loops of the as-deposited (top panel) and annealed (bottom panel) samples. Sample Co**90**-AD shows a net but small out-of-plane effective anisotropy, as it can be deduced from the increased value of remanence in the parallel field configuration, m_R (θ=0º)=0.46 instead of m_R(θ=90º)=0.35 (see Figure 6 (a)). On the other hand, samples Co**80**-AD and Co**70**-AD are remarkably similar and anisotropic (Figures 6 (b) and (c), respectively), with in-plane effective anisotropy. After annealing, samples Co**90**-TT and Co**80**-TT become almost isotropic (Figures 6 (d) and (e), respectively) while sample Co**70**-TT enhances its effective in-plane anisotropy (Figure 6 (f)).

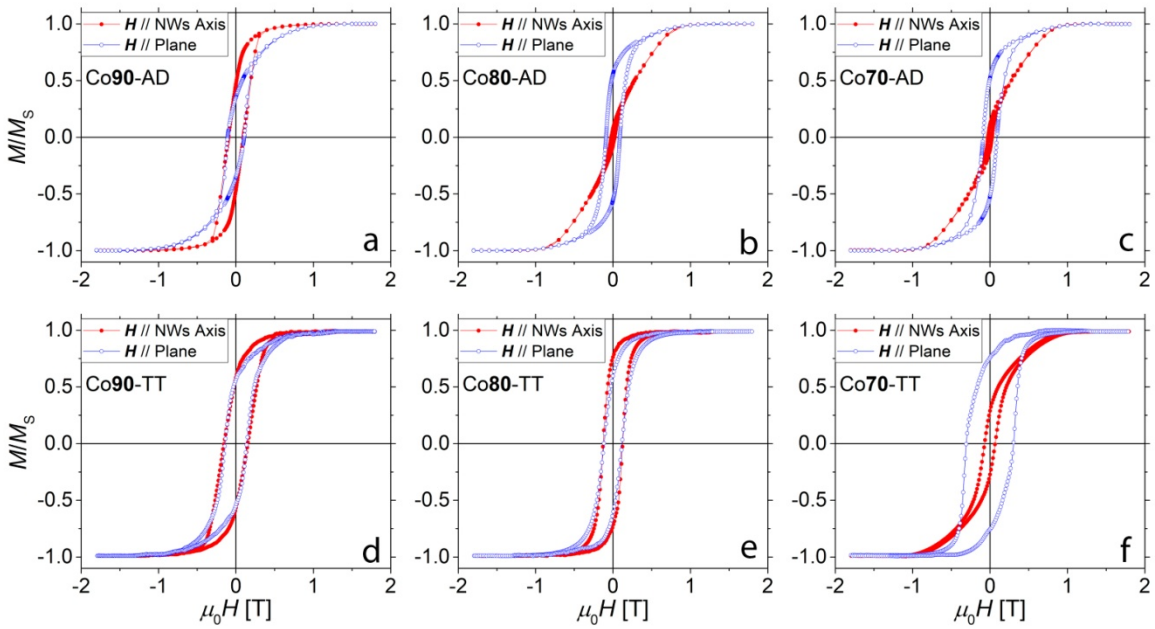

Figure 6. Hysteresis loops (top panel) before and (bottom panel) after annealing of samples (a) Co**90**-AD, (b) Co**80**-AD, (c) Co**70**-AD, (d) Co**90**-TT, (e) Co**80**-TT and (f) Co**70**-TT with the applied field ***H*** parallel to the NWs axis (θ=0º, solid circles) and parallel to the array's plane (θ=90º, open circles).

It is noteworthy that the magnetic behavior of the arrays changed after the annealing. Figure 7 displays both (top panel) $\mu_0 H_C$ vs. θ and (bottom panel) m_R vs. θ curves for (a, c) as-deposited and (b, d) thermally treated samples. The relative remanence mimics the coercivity behavior in every sample, being both of them maximized at the same angles. The magnetization easy axis (MEA) can be taken as the direction in which the largest coercivity (H_C^{MAX}) and relative remanence (m_R^{MAX}) are attained. For samples Co**80**-AD, Co**70**-AD and Co**70**-TT both H_C^{MAX} and m_R^{MAX} occur at θ=90º (the array's plane). On the contrary, samples Co**90**-AD and Co**90**-TT show a rather constant behavior for H_C and m_R, being magnetically isotropic. Lastly, sample Co**80**-TT also presents a constant behavior for H_C, but m_R^{MAX} is attained at θ= 0º (and θ= 180º), indicating that this is the direction of the MEA.

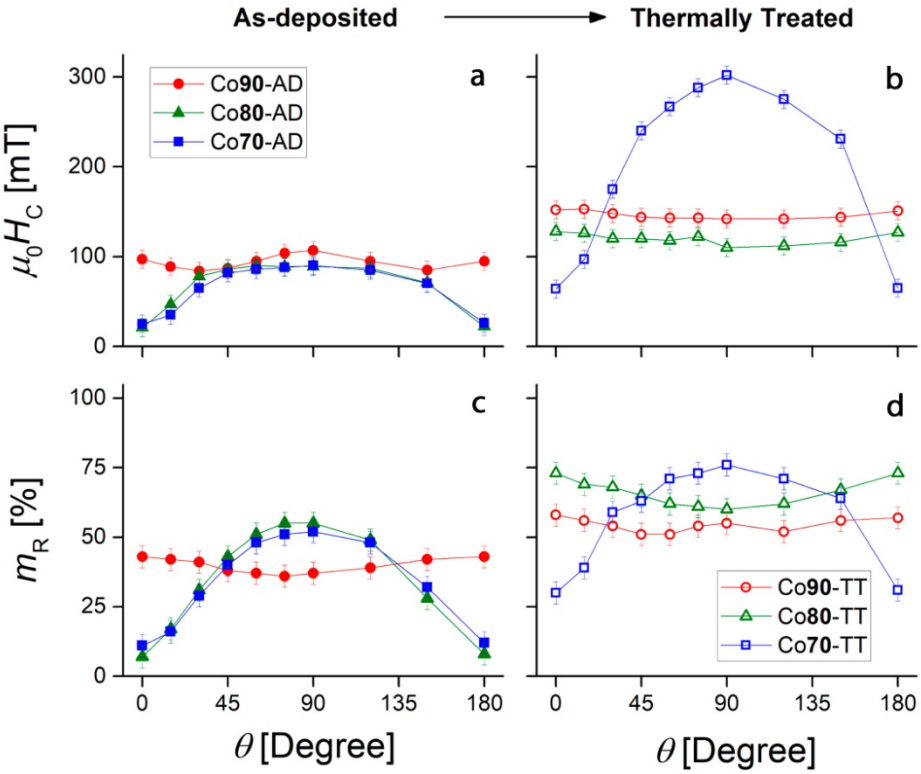

Figure 7.(Top panel) Coercivity and (bottom panel) relative remanence for the (a, c) as-deposited and (b, d) annealed NWs arrays as functions of the angle between the applied field and the NWs axis. As-deposited and thermally treated samples are represented by solid and open symbols, respectively. The compositions $Co_{90}Pt_{10}$, $Co_{80}Pt_{20}$ and $Co_{70}Pt_{30}$ are associated to circles, triangles and squares, respectively.

For all the as-deposited samples, $\mu_0 H_C^{MAX}$ was 100 mT when the field was applied parallel to the array's plane (θ=90º). After the thermal treatment, this value increased only slightly for samples Co**90**-TT and Co**80**-TT, but it tripled ($\mu_0 H_C^{MAX}$=300 mT) for Co**70**-TT. After annealing, m_R^{MAX} also increased, around 20 % in every case. These magnetic parameters, as well as the corresponding MEA are summarized in Table 3.

Table 3. Maximum values of coercivity and relative remanence, and the direction of the magnetization easy axis (MEA) for all samples.

Sample	$\mu_0 H_C^{MAX}$ [mT±10 mT]	m_R^{MAX} [% ± 3%]	MEA
Co**90**-AD	100	43	Isotropic
Co**90**-TT	150	58	Isotropic
Co**80**-AD	100	56	90º
Co**80**-TT	130	73	0º
Co**70**-AD	100	52	90º
Co**70**-TT	300	76	90º

4. Discussion

To further understand the magnetic behavior of each sample, its correlation with the corresponding crystalline structure must be taken into account. The general behavior of a NWs array is determined by the individual energetic contribution of each nanowire plus an interaction term [55–63]. We consider the shape anisotropy K_{shape}, which depends on the geometry of a single nanowire, the interaction anisotropy K_{inter},

conditioned by the magnetostatic coupling of the NWs in the array, and the crystalline anisotropy K_{crys}, which is subordinated to the phase structure and crystallographic texture. The energy equilibrium equation can be reduced to an effective anisotropy K_{eff}, which represents the total energy density of the system:

$$K_{eff} = K_{shape} + K_{inter} + K_{crys} \quad (1)$$

Here, shape and interaction terms are of magnetostatic origin. The shape energy density K_{shape} is proportional to the squared saturation magnetization M_S^2 and to the difference ΔN of the demagnetizing factors parallel and perpendicular to the NWs axis [64]:

$$K_{shape} = \frac{1}{2}\Delta N \mu_0 M_S^2. \quad (2)$$

A positive value of K_{shape} means that the direction favored by this anisotropy is the NWs axis, whereas a negative result favors the array's plane. For the NWs arrays studied in this work ΔN can be approximated by 0.5 (the maximum value for infinite cylindrical wires [64]) because of the high aspect ratio of the nanowires (see Table 1). For all samples, an upper bound for K_{shape} can be established using the saturation magnetization of pure Co ($\mu_0 M_S$ = 1.79 T [64]), giving K_{shape} = 637 kJ/m^3 and favoring the NWs axis as the MEA.

The interaction anisotropy K_{inter} has been previously modeled according to different theories. Here, we follow the model proposed by Encinas-Oropesa et al. [61] for a hexagonal NWs array:

$$K_{inter} = -\frac{\sqrt{3}}{8}\pi\left(\frac{d}{dcc}\right)^2 \mu_0 M_S^2, \quad (3)$$

where the negative sign indicates that this anisotropy favors the alignment of the magnetization parallel to the array's plane. Using d = 55 nm and dcc = 110 nm, an upper bound for the interaction energy density for all samples can be estimated with the saturation magnetization of pure Co, giving K_{inter} = - 434 kJ/m^3 and promoting an easy plane of magnetization perpendicular to the NWs axis. Thus, these two energy terms compete to determine the MEA, resulting in a net magnetostatic energy constant of about $K_0 = K_{inter} + K_{shape} \approx$ 203 kJ/m^3 along the NWs axis.

The crystalline anisotropy K_{crys} depends on the crystal symmetry and texture. For single-crystal *hcp* pure Co it is $K_{crys} \approx$ 450 kJ/m^3 [65], which is of the same order of magnitude than the previously calculated K_{shape} and K_{inter}. In this case, the MEA is determined by the "*c*" axis orientation, which is also related to the texture. On the other hand, for textured *fcc* Co the crystalline anisotropy can also reach high values, up to 270 kJ/m^3 [66–68]. If the sample is polycrystalline with no crystallographic texture, then the crystalline energy averages to zero.

For samples Co**90**-AD and Co**90**-TT, the angular dependence of coercivity and relative remanence observed in Figure 7 indicates a nearly isotropic behavior. Considering the three energy terms taken into account for K_{eff} (Eq. 1), we infer that the magnetocrystalline anisotropy balances the magnetostatic terms. The NWs arrays show a hexagonal crystallographic symmetry with texture in the (010) and (011) directions along the NWs axis (see Figure 5), which favor, respectively, the MEA in the array's plane and the direction at a given angle with that plane. Given the polycrystalline character of the NWs, there is not any preferred azimuthal direction. We can estimate the effective magnetocrystalline anisotropy constant as $K_{crys} \approx$ - 200 kJ/m^3 (i.e., in the array's plane), matching the magnitude of K_0. For this composition ($Co_{90}Pt_{10}$) the thermal treatment does not modify the isotropic behavior and both $\mu_0 H_C$ and m_R are only moderately increased. This could be ascribed to a slight relaxation of the crystallographic structure while keeping the same texture.

As shown in Table 3, samples Co**80**-AD and Co**80**-TT are the only ones that display a MEA transition from in-plane (AD) to out-of-plane (TT). Before annealing, the main crystallographic phase of Co**80**-AD is Co *hcp* with the "*c*" axis laying in the array's plane (K_{crys}<0). In this sample, the MEA is in the array's plane as a result of the magnetocrystalline anisotropy overcoming the axial magnetostatic contribution (- K_{crys}>K_0). After annealing, the crystalline structure completely transforms into cubic *fcc*, with no preferred crystallographic orientations. As a consequence, the magnetocrystalline anisotropy nearly vanishes and only the magnetostatic term K_0 remains, leading to a MEA aligned with the NWs axis.

In both samples Co**70**-AD and Co**70**-TT the MEA lays in the array's plane, denoting an effective in-plane anisotropy. Therefore, the magnitude of K_{crys} overcomes K_0 and has a negative value. It is noteworthy that even when both Co80-TT and Co70-TT show similar phase transitions to the *fcc* structure, Co80-TT has no preferential orientations, averaging K_{crys} to negligible values, while Co70-TT displays a crystallographic texture in the (111) direction which contributes to the enhanced in-plane magnetic anisotropy observed in this sample. Yamada et al. [22] found that for Co-Pt alloy thin films H_C shows a maximum at approximately 75 at.% Co content, both in-plane and in perpendicular directions. In the NWs arrays studied in this work, the maximum of effective magnetic

anisotropy this maximum is attained at a slightly lower Co content, the $Co_{70}Pt_{30}$ composition, resulting in the large coercivity observed for sample Co**70**-TT. Before annealing (sample Co**70**-AD) there was a coexistence of *hcp* and *fcc* crystallographic phases preventing the magnetocrystalline anisotropy from reaching a higher value.

Summing up, shape anisotropy with an upper bound of $K_{shape} \approx$ 640 kJ/m^3 always promotes a MEA in the NWs axis direction, while the interaction anisotropy $K_{inter} \approx$- 440 kJ/m^3 (lower bound) favors a magnetization in the array's plane, and they compete to define the effective MEA. However, the magnetocrystalline anisotropy K_{crys} can balance or unbalance the equation depending on the crystalline phases and the crystallographic textures. Consequently, the magnetic effective anisotropy K_{eff} of the NWs array can be controlled by selecting the Co content –from 90 to 70 at.%– and the thermal treatment. Previous works on Co-Pt NWs arrays with diameter smaller than 100 nm never showed an in-plane magnetic anisotropy ($K_{eff} < 0$). To the best of our knowledge, we are the first to achieve this feature for Co**80**-AD, Co**70**-AD and Co**70**-TT samples, which also present enhanced coercivity and remanence as compared to thicker NWs and thin films of different compositions, ranging from $Co_{90}Pt_{10}$ to $Co_{40}Pt_{60}$ [22,32,34,38,39,44–46].

5. Conclusion

Arrays of Co_xPt_{100-x} (x= 90, 80, 70) NWs of 55 nm diameter were synthesized by electrodeposition, using nanoporous alumina templates. Thermal treatments at 500 ºC in Ar atmosphere were performed looking for the stabilization of metastable phases and phase transitions. The analysis of the crystalline phases for each sample showed that the *hcp* and/or *fcc* phases were obtained according to the composition and annealing, in agreement with the phase diagram for this alloy.

The magnetically isotropic behavior in samples Co**90**-AD and Co**90**-TT is ascribed to the balance between magnetostatic and crystalline terms in both samples. On the other hand, the in-plane magnetic anisotropy of sample Co**80**-AD is related to the *hcp* crystalline structure, textured in the array's plane, while after annealing (Co**80**-TT) the crystalline structure completely transforms into *fcc* phase with no crystallographic texture, resulting in a slightly anisotropic magnetic behavior, favoring the NWs axis direction. Samples Co**70**-AD and Co**70**-TT are textured in the array's plane, leading to an in-plane magnetic anisotropy. The remarkable hardening of Co**70**-TT may arise from the crystallographic transformation from *hcp* to *fcc* phase.

Acknowledgments

This work has been performed within the framework of the i-COOPB20307 project supported by the Spanish National Council for Research, CSIC. Financial supports of the Regional Government of Madrid under the project S2018/NMT-4321 NANOMAGCOST-CM, the Spanish Ministry of Economy, Industry and Competitiveness (MINECO) under project MAT2016-76824-C3-1-R and Foncyt (Argentina) under project PICT-2015-0135 are also acknowledged. The authors declare that they have no conflict of interests.

Data availability

The data that support the findings of this study are available on request from the corresponding author.

References

[1] Z. Liu, P.-W. Huang, S. Hernandez, G. Ju, T. Rausch, Systematic evaluation of microwave-assisted magnetic recording, IEEE Trans. Magn. 54 (2018) 1–5.

[2] G. Barucca, T. Speliotis, G. Giannopoulos, D. Niarchos, B. Rutkowski, A. Czyrska-Filemonowicz, E. Agostinelli, S. Laureti, A.M. Testa, G. Varvaro, Magnetic anisotropy phase-graded A1/$L1_0$-FePt films on amorphous glass substrates, Mater. Des. 123 (2017) 147–153.

[3] K. Wang, X. Zhu, G. Ju, K.C. Chang, Y. Peng, T.J. Klemmer, J.-U. Thiele, Heat-assisted rotating disk magnetometer for ultra-high anisotropy magnetic measurements, 2016. US Patent 9,336,832.

[4] A. Stupakiewicz, K. Szerenos, M.D. Davydova, K.A. Zvezdin, A.K. Zvezdin, A. Kirilyuk, A. V Kimel, Selection rules for all-optical magnetic recording in iron garnet, Nat. Commun. 10 (2019) 612.

[5] A. Stupakiewicz, K. Szerenos, D. Afanasiev, A. Kirilyuk, A. V Kimel, Ultrafast nonthermal photo-magnetic recording in a transparent medium, Nature. 542 (2017) 71.

[6] G.P. Zhang, Y.H. Bai, T.F. George, Is perpendicular magnetic anisotropy essential to all-optical ultrafast spin reversal in ferromagnets?, J. Phys. Condens. Matter. 29 (2017) 425801.

[7] Y. Fuji, S. Kaji, M. Hara, Y. Higashi, A. Hori, K. Okamoto, T. Nagata, S. Baba, A. Yuzawa, K. Otsu, others, Highly sensitive spintronic strain-gauge sensor based on a MgO magnetic tunnel junction with an amorphous CoFeB sensing layer, Appl. Phys. Lett. 112 (2018) 62405.

[8] J.A. Munoz, D.E. Nikonov, K.J. Kuhn, P. Theofanis, C. Pawashe, K. Lin, S. Kim, Magnetic nanomechanical devices for stiction compensation, (2018). US Patent 9,926,19.

[9] J. Lee, J. Yoo, S. Min, M. Yoon, Topology optimization of anisotropic magnetic composites in actuators using

homogenization design method, Struct. Multidiscip. Optim. (2019) 1–14.
[10] C. Schopphoven, A. Tschöpe, Magnetic anisotropy of nickel nanorods and the mechanical torque in an elastic environment, J. Phys. D. Appl. Phys. 51 (2018) 115005.
[11] L.K. Quynh, B.D. Tu, C. V Anh, N.H. Duc, A.T. Phung, T.T. Dung, D.T.H. Giang, Design Optimization of an Anisotropic Magnetoresistance Sensor for Detection of Magnetic Nanoparticles, J. Electron. Mater. 48 (2019) 997–1004.
[12] Y. Guo, Y. Ouyang, N. Sato, C.C. Ooi, S.X. Wang, Exchange-biased anisotropic magnetoresistive field sensor, IEEE Sens. J. 17 (2017) 3309–3315.
[13] A. Kamra, D.M. Polishchuk, V. Korenivski, A. Brataas, Anisotropic and Controllable Gilbert-Bloch Dissipation in Spin Valves, Phys. Rev. Lett. 122 (2019) 147201.
[14] A.G. Kolesnikov, H. Wu, M.E. Stebliy, A. V Ognev, L.A. Chebotkevich, A.S. Samardak, X. Han, Hybrid magnetic anisotropy $[Co/Ni]_{15}/Cu/[Co/Pt]_4$ spin-valves, J. Magn. Magn. Mater. 449 (2018) 271–277.
[15] N. Kikuchi, O. Kitakami, S. Okamoto, Y. Shimada, A. Sakuma, Y. Otani, K. Fukamichi, Influence of 5d transition elements on the magnetocrystalline anisotropy of hexagonal close-packed Co, J. Phys. Condens. Matter. 11 (1999) L541--L546.
[16] A. Sakuma, First principle calculation of the magnetocrystalline anisotropy energy of FePt and CoPt ordered alloys, J. Phys. Soc. Japan. 63 (1994) 3053–3058.
[17] G.H.O. Daalderop, P.J. Kelly, M.F.H. Schuurmans, Magnetocrystalline anisotropy and orbital moments in transition-metal compounds, Phys. Rev. B. 44 (1991) 12054.
[18] Q.F. Xiao, E. Brück, Z.D. Zhang, F.R. De Boer, K.H.J. Buschow, Phase transformation and magnetic properties of bulk CoPt alloy, J. Alloys Compd. 364 (2004) 64–71.
[19] F. Bolzoni, F. Leccabue, R. Panizzieri, L. Pareti, Magnetocrystalline anisotropy and phase transformation in Co-Pt alloy, IEEE Trans. Magn. 20 (1984) 1625–1627.
[20] M. Abes, O. Ersen, D. Muller, M. Acosta, C. Ulhaq-Bouillet, A. Dinia, V. Pierron-Bohnes, Effect of ion irradiation on the structural and magnetic properties of sputtered CoPt alloy, Mater. Sci. Eng. C. 23 (2003) 229–233.
[21] M. Maret, M.C. Cadeville, W. Staiger, E. Beaurepaire, R. Poinsot, A. Herr, Perpendicular magnetic anisotropy in Co_xPt_{1-x} alloy films, Thin Solid Films. 275 (1996) 224–227.
[22] Y. Yamada, T. Suzuki, E.N. Abarra, Magnetic properties of electron beam evaporated CoPt alloy thin films, IEEE Trans. Magn. 33 (1997) 3622–3624.
[23] H. Li, C. Xu, G. Zhao, Y. Su, T. Xu, H. Li, Fabrication and magnetic properties of amorphous $Co_{0.71}Pt_{0.29}$ nanowire arrays, Solid State Commun. 132 (2004) 399–403.
[24] J. Mallet, K. Yu-Zhang, C.-L. Chien, T.S. Eagleton, P.C. Searson, Fabrication and magnetic properties of fcc Co_XPt_{1-X} nanowires, Appl. Phys. Lett. 84 (2004) 3900–3902.
[25] Z. Zhang, D.A. Blom, Z. Gai, J.R. Thompson, J. Shen, S. Dai, High-yield solvothermal formation of magnetic CoPt alloy nanowires, J. Am. Chem. Soc. 125 (2003) 7528–7529.
[26] S.H. Kim, T.H. Lee, Z.H. Jang, K.-Y. Choi, B.J. Suh, Magnetic Anisotropy Energy Barrier Distribution and Surface Magnetism in CoPt Nanoparticle, J. Korean Phys. Soc. 74 (2019) 261–268.
[27] X. Meng, H.C. Seton, L.T. Lu, I.A. Prior, N.T.K. Thanh, B. Song, Magnetic CoPt nanoparticles as MRI contrast agent for transplanted neural stem cells detection, Nanoscale. 3 (2011) 977–984.
[28] F. Tournus, N. Blanc, A. Tamion, M. Hillenkamp, V. Dupuis, Synthesis and magnetic properties of size-selected CoPt nanoparticles, J. Magn. Magn. Mater. 323 (2011) 1868–1872.
[29] F. Tournus, N. Blanc, A. Tamion, M. Hillenkamp, V. Dupuis, Dispersion of magnetic anisotropy in size-selected CoPt clusters, Phys. Rev. B. 81 (2010) 220405.
[30] F. Tournus, S. Rohart, V. Dupuis, Magnetic anisotropy dispersion in CoPt nanoparticles: An evaluation using the Néel model, Ieee Trans. Magn. 44 (2008) 3201–3204.
[31] S. Mourdikoudis, K. Simeonidis, K. Gloystein, M. Angelakeris, C. Dendrinou-Samara, I. Tsiaoussis, O. Kalogirou, Tailoring the morphology of Co_xPt_{1-x} magnetic nanostructures, J. Magn. Magn. Mater. 321 (2009) 3120–3125.
[32] B. Das, M. Mandal, K. Mandal, P. Sen, Influence of alumina membrane on magnetic properties for thermally annealed CoPt alloy nanowires, Colloids Surfaces A Physicochem. Eng. Asp. 443 (2014) 398–403.
[33] B. He, X. Meng, Q. Tang, Low-cost counter electrodes from CoPt alloys for efficient dye-sensitized solar cells, ACS Appl. Mater. Interfaces. 6 (2014) 4812–4818.
[34] M. Cortes, E. Gomez, E. Vallés, Electrochemical growth of CoPt nanowires of different aspect ratio and their magnetic properties, J. Electroanal. Chem. 689 (2013) 69–75.
[35] H. Khurshid, Y.H. Huang, M.J. Bonder, G.C. Hadjipanayis, Microstructural and magnetic properties of CoPt nanowires, J. Magn. Magn. Mater. 321 (2009) 277–280.
[36] Y. Dahmane, L. Cagnon, J. Voiron, S. Pairis, M. Bacia, L. Ortega, N. Benbrahim, A. Kadri, Magnetic and structural properties of electrodeposited CoPt and FePt nanowires in nanoporous alumina templates, J. Phys. D. Appl. Phys. 39 (2006) 4523.
[37] J. Rivas, A.K.M. Bantu, G. Zaragoza, M.C. Blanco, M.A. López-Quintela, Preparation and magnetic behavior of arrays of electrodeposited Co nanowires, J. Magn. Magn. Mater. 249 (2002) 220–227.
[38] S. Shamaila, R. Sharif, S. Riaz, M. Ma, M. Khaleeq-ur-Rahman, X.F. Han, Magnetic and magnetization properties of electrodeposited fcc CoPt nanowire arrays, J. Magn. Magn. Mater. 320 (2008) 1803–1809.
[39] K. Barmak, J. Kim, L.H. Lewis, K.R. Coffey, M.F. Toney, A.J. Kellock, J.-U. Thiele, On the relationship of

magnetocrystalline anisotropy and stoichiometry in epitaxial $L1_0$ CoPt (001) and FePt (001) thin films, J. Appl. Phys. 98 (2005) 33904.
[40] M. Maret, M.C. Cadeville, A. Herr, R. Poinsot, E. Beaurepaire, S. Lefebvre, M. Bessiere, Enhanced perpendicular magnetic anisotropy in chemically long-range ordered (0001) Co_xPt_{1-x} films, J. Magn. Magn. Mater. 191 (1999) 61–71.
[41] S. Shamaila, R. Sharif, J.Y. Chen, H.R. Liu, X.F. Han, Magnetic field annealing dependent magnetic properties of $Co_{90}Pt_{10}$ nanowire arrays, J. Magn. Magn. Mater. 321 (2009) 3984–3989.
[42] W. Li, Y. Peng, G.A. Jones, T.H. Shen, G. Hill, Co-rich cobalt platinum nanowire arrays: Effects of annealing, J. Appl. Phys. 97 (2005) 34308.
[43] W. Li, T.H. Shen, Composition and annealing temperature dependent properties of $Co_{1-x}Pt_x$ (0< x□ 0.2) alloy nanowire arrays, J. Appl. Phys. 97 (2005) 10J706.
[44] M. Ohtake, S. Ouchi, F. Kirino, M. Futamoto, Structure and magnetic properties of CoPt, CoPd, FePt, and FePd alloy thin films formed on MgO (111) substrates, IEEE Trans. Magn. 48 (2012) 3595–3598.
[45] D. Suzuki, M. Ohtake, F. Kirino, M. Futamoto, Preparation of CoPt-Alloy Thin Films With Perpendicular Magnetic Anisotropy on MgO (111), $SrTiO_3$ (111), and Al_2O_3 (0001) Single-Crystal Substrates, IEEE Trans. Magn. 48 (2012) 3195–3198.
[46] F.-T. Yuan, J.-H. Hsu, Y.-H. Lin, S.N. Hsiao, H.Y. Lee, Structural studies of high-K u metastable CoPt thin films with long-range order, J. Appl. Phys. 111 (2012) 07A303.
[47] C. Bran, E.M. Palmero, Z.-A. Li, R.P. Del Real, M. Spasova, M. Farle, M. Vázquez, Correlation between structure and magnetic properties in Co_xFe_{100-x} nanowires: the roles of composition and wire diameter, J. Phys. D. Appl. Phys. 48 (2015) 145304.
[48] B. Rodríguez-González, C. Bran, T. Warnatz, J. Rivas, M. Vazquez, Structural and magnetic characterization of as-prepared and annealed FeCoCu nanowire arrays in ordered anodic aluminum oxide templates, J. Appl. Phys. 115 (2014). https://doi.org/10.1063/1.4870289.
[49] W.M. Haynes, CRC Handbook of Chemistry and Physics 2013-2014, CRC Press. (2013).
[50] A.S.M. Handbook, Alloy phase diagrams, ASM Int. 3 (1992).
[51] A.L. Patterson, The Scherrer formula for X-ray particle size determination, Phys. Rev. 56 (1939) 978.
[52] J.S. Kasper, K. Lonsdale, International Tables for X-Ray Crystallography. Volume II., Kinoch Press, Birmingham, UK, Birmingham, UK, 1972.
[53] N. Adeela, K. Maaz, U. Khan, S. Karim, M. Ahmad, M. Iqbal, S. Riaz, X.F. Han, M. Maqbool, Fabrication and temperature dependent magnetic properties of nickel nanowires embedded in alumina templates, Ceram. Int. 41 (2015) 12081–12086.
[54] W.P. Davey, Precision measurements of the lattice constants of twelve common metals, Phys. Rev. 25 (1925) 753–761. https://doi.org/10.1103/PhysRev.25.753.
[55] J.D.L.T. Medina, G. Hamoir, Y. Velázquez-Galván, S. Pouget, H. Okuno, L. Vila, A. Encinas, L. Piraux, Large magnetic anisotropy enhancement in size controlled Ni nanowires electrodeposited into nanoporous alumina templates, Nanotechnology. 27 (2016) 145702.
[56] C. Bran, A.P. Espejo, E.M. Palmero, J. Escrig, M. Vázquez, Angular dependence of coercivity with temperature in Co-based nanowires, J. Magn. Magn. Mater. 396 (2015) 327–332.
[57] L. Piraux, G. Hamoir, A. Encinas, J. De La Torre Medina, F. Abreu Araujo, Influence of the packing fraction and host matrix on the magnetoelastic anisotropy in Ni nanowire composite arrays, J. Appl. Phys. 114 (2013) 123907.
[58] K.M. Razeeb, F.M.F. Rhen, S. Roy, Magnetic properties of nickel nanowires: Effect of deposition temperature, J. Appl. Phys. 105 (2009) 1–7.
[59] a. Kumar, S. Fähler, H. Schlörb, K. Leistner, L. Schultz, Competition between shape anisotropy and magnetoelastic anisotropy in Ni nanowires electrodeposited within alumina templates, Phys. Rev. B - Condens. Matter Mater. Phys. 73 (2006) 1–5.
[60] M. Vázquez, K. Pirota, J. Torrejón, D. Navas, M. Hernández-Vélez, Magnetic behaviour of densely packed hexagonal arrays of Ni nanowires: Influence of geometric characteristics, J. Magn. Magn. Mater. 294 (2005) 174–181.
[61] A. Encinas-Oropesa, M. Demand, L. Piraux, I. Huynen, U. Ebels, Dipolar interactions in arrays of nickel nanowires studied by ferromagnetic resonance, Phys. Rev. B. 63 (2001) 104415.
[62] K. Nielsch, R.B. Wehrspohn, J. Barthel, J. Kirschner, U. Gösele, S.F. Fischer, H. Kronmüller, Hexagonally ordered 100 nm period nickel nanowire arrays, Appl. Phys. Lett. 79 (2001) 1360–1362.
[63] H. Schwanbeck, U. Schmidt, Preparation and characterisation of magnetic nanostructures using filtration membranes, Electrochim. Acta. 45 (2000) 4389–4398.
[64] B.D. Cullity, C.D. Graham, Introduction to magnetic materials, John Wiley & Sons, 2011.
[65] R. Ferré, K. Ounadjela, J.M. George, L. Piraux, S. Dubois, Magnetization processes in nickel and cobalt electrodeposited nanowires, Phys. Rev. B. 56 (1997) 14066.
[66] L.G. Vivas, R. Yanes, O. Chubykalo-Fesenko, M. Vazquez, Coercivity of ordered arrays of magnetic Co nanowires with controlled variable lengths, Appl. Phys. Lett. 98 (2011) 232507.
[67] J.P. Chen, C.M. Sorensen, K.J. Klabunde, G.C. Hadjipanayis, Magnetic properties of nanophase cobalt particles synthesized in inversed micelles, J. Appl. Phys. 76 (1994) 6316–6318.
[68] W. Sucksmith, J.E. Thompson, The magnetic anisotropy of cobalt, Proc. R. Soc. London. Ser. A. Math. Phys. Sci. 225 (1954) 362–375.